Magnetoresponsive Devices with Programmable Behavior Using a Customized Commercial Stereolithographic 3D Printer

Simone Lantean, Ignazio Roppolo, Marco Sangermano, Marc Hayoun, Hichem Dammak, Gabriele Barrera, Paola Tiberto, Candido Fabrizio Pirri, Laurence Bodelot, Giancarlo Rizza

Adv. Mater. Technol. **2022**, 2200288 **DOI: 10.1002/admt.202200288**

Magnetoresponsive Devices with Programmable Behavior Using a Customized Commercial Stereolithographic 3D Printer

Simone Lantean [1,2], Ignazio Roppolo [1,3*], Marco Sangermano[1], Marc Hayoun[2], Hichem Dammak [2,4], Gabriele Barrera[5], Paola Tiberto[5], Candido Fabrizio Pirri[1,3], Laurence Bodelot[6], Giancarlo Rizza[2]

1. Department of Applied Science and Technology, Politecnico di Torino, Duca degli Abruzzi, 24, 10124, Torino, Italy
2. Laboratoire des Solides Irradiés (LSI), Institut Polytechnique de Paris, CEA/DRF/IRAMIS, CNRS, Ecole polytechnique, Route de Saclay, 91128 Palaiseau, France
3. Center for Sustainable Future Technologies, Istituto Italiano di Tecnologia, Via Livorno 60, 10144, Torino, Italy
4. Laboratoire Structures Propriétés et Modélisation des Solides, CentraleSupélec, CNRS, Université Paris-Saclay, F 91190 Gif-sur-Yvette, France
5. Advanced Materials for Metrology and Life Sciences Division INRiM Strada delle Cacce 91, 10143 Torino, Italy
6. Laboratoire de Mécanique des Solides (LMS), CNRS, École polytechnique, Institut Polytechnique de Paris, Route de Saclay, 91128 Palaiseau, France

E-mail: ignazio.roppolo@polito.it

Keywords: 4D printing, magnetic device, programmed microstructure, magnetic actuation

Abstract

(text. 12 point, double-spaced. Maximum length 200 words. Written in the present tense.)

The revolution of 4D printing allows combining smart materials to additive processes to create behavioral objects able to respond to external stimuli, such as temperature, light, electrical or magnetic fields. Here, we used a modified commercial Digital Light Processing (DLP) 3D printer to obtain complex macroscopic remotely-controlled gear-based devices. The fabrication process is based on the printing of magneto-responsive polymers containing *in situ* self-assembled microstructures, i.e. composed of oriented chains of Fe_3O_4 nanoparticles. First, we demonstrate that we are able to print magneto-responsive hammer-like actuators with different stiffness allowing both pure rotation or/and bending motions. Then, we exploit microstructure to create a magneto-responsive gear. In particular, we showed that they can be successfully used to transfer torque to other gears, thereby converting a rotation movement into linear translation. Finally, we demonstrated that magneto-responsive gears can be also combined with

other non-magnetic elements to create complex assemblies, such as gear-trains, linear actuators and grippers, that can be remotely controlled.

1. Introduction

Materials science is continuously inspired by Nature. Millions of years of evolution led living matter to develop an endless number of architectures and peculiar properties, as the ability to undergo motion in response to environmental stimuli [1,2]. For instance, in abalone shells and shrimps the oriented and hierarchical microstructure is responsible for their outstanding impact resistance [3,4], in carnivorous plants, as the Dionaea muscipula, the micro-structure is exploited to induce precise shape morphism, in pinecones the motion is actuated in response to humidity [5–9]. Magnetotactic bacteria synthesize magnetic iron nanominerals inside them, which function as tiny compasses allowing them to navigate by means of Earth's geomagnetic field. [10] From a technical point of view, despite the attempts to mimic and reproduce natural architectures and patterns, conventional fabrication techniques often face technical and resolution limitations. In the last years, this gap is being partially bridged thanks to the development of the 3D printing, where starting from a Computer-Aided Design (CAD) file, the final object is built through the additive deposition of material sub-units. However, the real breakthrough in this field of research has been to first imagine and then print behavioral objects [11]. This is the domain of the so-called 4D printing, which is, in a way, the functional form of 3D printing [12–14]. Instead of printing only static objects, it becomes possible to print functions. This paradigm shift allows a printed object to adapt to its environment and to evolve in a controlled way through the application of stimuli. So far, the 4D printing approach has been applied to functional polymers or composite materials such as hydrogels [15–18], electroactive polymers [19–21], shape memory polymers [22–26], or polymers sensitive to pH [27,28] and light [29,30]. Yet, the research on 4D printed objects with controlled microstructure is still in its infancy and it mainly focuses on the fabrication of composite materials with enhanced mechanical properties [31–40], where only a few works mentions the possibility to control the microstructure *in situ* during the printing process [41–46]. In particular, we are interested here in the tailor-made printing of magneto-reactive composite polymers [47–49]. Indeed, they can be easily actuated by remote magnetic fields without damaging tissues and organs, and thus, by used for instance in soft robotics for healthcare and biomedical applications [50,51]. A first strategy to print magneto-responsive composite polymers consists in using hard magnetic fillers, such as $Nd_2Fe_{14}B$ micro-particles, and to orient their permanent dipoles using external strong magnets [52–54]. This process has

been mainly applied in Fused Filament Fabrication (FFF) and Direct Ink Writing (DIW) 3D printing techniques [53,55]. However, despite the fabrication of large objects in the X-Y plane, layer-to-layer adhesion issues generally limit their thickness to a few hundred microns [55]. A second strategy exploits the self-assembly of soft magnetic fillers, such as Fe_3O_4 nanoparticles (NPs) [56–58]. In particular, when soft magnetic fillers are dispersed within a liquid medium and exposed to an external field, they spontaneously assemble into chain-like filamentary structures aligned along the field vector. The dimension and direction of the assembled chains, i.e. , the microstructure, can be programed by varying the experimental parameters such as the intensity of the applied magnetic field, the NPs concentration, and the viscosity of the medium [59–61]. Finally, the microstructure can be frozen-in by curing the formulation, embedding it [60–62]. This creates a uniaxial magnetic anisotropy characterized by a magnetic easy axis (i.e., the major axis of the chains) along which the magnetic moments of single NPs are preferentially oriented, thereby forming an extended magnetic dipole in the chain [60–62]. This property can be exploited to actuate the printed object. Indeed, if an angle exists between the applied external magnetic field and the magnetic easy axis of the chains, a torque is exerted, which forces the object to rotate to align itself along the field vector [62–64]. Therefore, controlling the orientation of the magnetic microstructure allows programming the rotation and bending movements of the printed objects. So far, this approach has been mainly employed in 2D fabrication processes [65–68], in particular using a photo-lithographic approach, with the fabrication of multi-modal micro actuators [69]. More recently, the self-assembly process has also been applied to control the microstructure of twist-type micro-swimmers fabricated by Direct Laser Writing and actuated by external rotating fields [70–74], or to fabricate cellularized magneto-responsive hybrid hydrogels using a 3D bio-printing technique [75].

The present work bedrocks on the knowledge we developed so far in the formulation of photocurable magneto-active acrylic resins [76], as well as the *in situ* control of the self-assembly of magnetite (Fe_3O_4) NPs during the printing process [77]. Here, our erstwhile knowledge is exploited to create macroscopic complex assemblies of magneto-driven elements, that can be remotely controlled. This is done in three steps: first, the formation of a controlled microstructure through the self-assembly of Fe_3O_4 NPs dispersed in photocurable resins as well as its spatial orientation have been investigated and rationalized by using numerical simulations. Second, we modified a commercial DLP printer [77] to obtain complex magneto-responsive objects, whose magnetic and mechanical properties have been measured for different formulations of the resin, the overall content of magnetic fillers and the spatial orientation of the microstructure. Finally, as a proof-of-concept, we fabricated different magneto-responsive

devices: hammer-like actuators with different stiffnesses, as well as magneto-responsive gears. Finally, we combined magneto-responsive components with non-magnetic elements to create complex assemblies, such as gear-trains, linear actuators and grippers, that can be remotely controlled.

2. Experimental

2.1 Formulation

The magneto-active formulation is obtained by adding magnetite nanoparticles (Fe_3O_4 NPs, 50-100 nm diameter) to a photocurable Urethane Acrylate resin (Ebecryl® 8232) with different amount of Butyl Acrylate (BA), as reported in [76]. As demonstrated in previous work, this last ingredient is used both to adjust the viscosity of the formulation and to control the mechanical properties. In particular, three different weight concentrations of BA have been considered (0%, 25%, and 50%), leading to three different formulations, hereafter named as 100Eb, 75Eb25BA, and 50Eb50BA. Their corresponding viscosity has been measured to be η=5.6 Pa.s, η=1.8 Pa.s, and η=0.02 Pa.s. Viscosity and photo-reactivity of the formulations have been used to tune both the mechanical properties of the printed object as well as the dimensions of the embedded chain-like aggregates of Fe_3O_4 NPs as reported in [77].

2.2 Self-assembly-driven magnetic microstructure

The average length of the self-assembled chains, their spatial orientation, and the concentration of the loaded magnetic fillers have been studied *in situ* using a Leica DFC295 optical microscope equipped with a 10x optics, and experimental results have been rationalized by using numerical simulations based on a dipolar approximation model [77-79]. The viscosity effect has been investigated for the 75Eb25BA and 50Eb50BA formulations by coating, with the help of a wire wound bar, a 200 μm thick film on the surface of a microscope slide. This thickness has been chosen to mimic 10 layers (20 μm each) of a printed sample.

The orientation step is triggered by applying a 10 mT magnetic field in the horizontal direction ($\theta_B = 0$) for 180 s for the chains to reach stable dimension[77]. Then, the magnetic field is rotated by $\theta_B = 30°$ and the image taken 120 s after the rotation step. Experimental results have been coupled to numerical simulations on a system composed of 1,000 NPs using periodic

boundary conditions [78,79]. The size of the cubic box depends on the weight fraction of NPs. More details can be found in the Supporting Information File.

2.3 DLP printer modification and printing parameters

The control of the microstructure within the printed composite polymers is obtained by using a modified DLP machine (RobotFactory HD 2.0+) as described in [77]. As shown in Fig. 1a-b, a linear-to-rotary actuator driven by an Arduino microcontroller is used to control the rotation of a non-magnetic ball-bearing glued on the bottom glass plate of the vat. Its role is twofold: i) the central hole acts as a resin reservoir, while ii) the rotating external wall is used to apply the magnetic field in the X-Y plane (H) by fixing to it two permanent magnets of suitable intensity. The intensity of the applied magnetic field has been tested by considering several combinations of permanent magnets, hereafter named as A and B (www.supermagnete.fr). The A magnet is a 60x10x2 mm^3 parallelepiped exhibiting a magnetic field at the surface of 120 mT, while the B magnet is a 40x10x5 mm^3 parallelepiped exhibiting a magnetic field at the surface of 310 mT. Finally, to fit with the new resin reservoir, the original building platform was modified by adding an appropriately sized glass cylinder.

The processing parameters have been determined for 75Eb25BA and 50Eb50BA formulations by printing rectangular samples (3 mm thick) for increasing concentration of Fe_3O_4 NPs (up to 8 wt.%) in the absence and presence of magnetic field, i.e., B=0 mT and B=10 mT, respectively. The thickness of each printed layer was set to be 20 µm. Table 1 reports the processing parameters for the different formulations. All the different structures tested along the manuscript where 3D printed following these parameters.

Table 1: Printing parameters used to 3D print the magneto composite polymers.

Sample	Alignment Magnetic field (mT)		Slicing (µm)	Base exposing time (s)	Object exposing time (s)
75Eb25BA_2wt.%NPs	0	10	20	2.9	1.6
75Eb25BA_4wt.%NPs	0	10	20	4.4	2
75Eb25BA_6wt.%NPs	0	10	20	5.8	2.4
75Eb25BA_8wt.%NPs	0	10	20	9.5	3
50Eb50BA_2wt.%NPs	0	10	20	2.9	1.4
50Eb50BA_4wt.%NPs	0	10	20	4.2	1.8
50Eb50BA_6wt.%NPs	0	10	20	5.5	2.2
50Eb50BA_8wt.%NPs	0	10	20	9.5	3

2.4 Characterization

The dispersion of magnetic fillers as well as their self-assembly in chains was investigated by using a Zeiss Supra 40 Field Emission Scanning Electron Microscopy (FESEM). Cryo-fracturing of photocured samples was used to avoid plastic deformation and filamentary aggregates.

The magnetic properties of the 3D printed objects have been investigated at room temperature by an Alternating Gradient Field Magnetometer (AGFM) operating with an applied magnetic field in the range -1.5 T up to +1.5 T. The hysteresis loops (i.e., the magnetization *vs.* applied magnetic field curves, M(H)) have been measured along the three symmetry equivalent directions—hereafter named as parallel (x-direction), transverse (y-direction), and perpendicular (z-direction) of a 3D printed cubic sample (3x3x3 mm^3). All magnetic curves have been normalized to the magnetic moment value at H = 1.5 T.

The hysteresis curve allows to evaluate the magnetic susceptibility, χ, which is defined by $\chi = M/H$. It describes the way in which M varies within the material as a function of the applied field H. As χ is a tensor, it can be used to estimate the magnetic behavior of the sample along different spatial directions. Here, the magnetic susceptibility measured at the coercive field of the hysteresis curve $\chi_c(H_c)$ has been selected as a physical indicator to estimate the degree of magnetic anisotropy in the sample.

Two microstructural configurations of printed samples loaded with 6 wt.% of Fe_3O_4 NPs have been investigated : i) randomly distributed NPs, and ii) self-assembled chains. For the latter, chains are created during the additive step by applying a magnetic field of 10 mT in the x-y plane along three different directions, 0°, 45°, or 90° with respect to the x-direction.

Vector-Vibrating Sample Magnetometer (V-VSM) was used to study the angular dependence of the magnetic anisotropy in both samples. In particular, the component of magnetization ($M\perp$) perpendicular to the direction of the applied magnetic field was measured as a function of the angle during the relative rotation of the sample. To this end, samples with both randomly and filamentary distributed NPs were 3D printed with a cylindrical shape to avoid any magnetic anisotropy effect.

Dynamic Mechanical Thermal Analysis (DMTA) in tensile configuration (Triton Technology TTDMA equipment) was used to measure mechanical properties. Elongation tests were run at

room temperature in load control (1N/min). The dimensions of the tested specimens are 30x4x3 mm^3 (length x width x thickness) with chains oriented at 0°, 45°, and 90° relative to the length of the sample. For comparison, 3D printed samples with randomly dispersed NPs are used as reference.

3D scanning of the 3D printed object was performed with a E3 scanner (3shape). The comparison heat map was obtained by the Convince software (3shape).

3.2 Result and Discussion

The optimum condition to print magneto-responsive composite materials depends on three parameters: i) the average length of the self-assembled chains, ii) their spatial orientation, and iii) the concentration of the loaded magnetic fillers [77]. Figure SI1 illustrates the time evolution of the average length of self-assembled chains when exposed to a magnetic field of 10 mT. Here, the timeframe is limited to 180 s to be compatible with the printing process, and each point represents the average of at least 200 measurements. For both formulations, the chains' length reaches a plateau within 180 s; however, their values are quite different. Indeed, the formulation having the lower viscosity (50Eb50BA and open circles) leads to the formation of chains that are more than twice as long, i.e., ~50 μm, than those formed in the more viscous formulation (75Eb25BA and full circles), i.e., ~20 μm.

Once the chains of magnetic fillers have reached their saturation length, the microstructure can be spatially oriented by rotating the magnetic field. In this case, the aggregates will be submitted to a torque that will force the chains to re-orient their magnetic dipoles along the direction of the applied field [61,80–84], see Figure S1, for the 50Eb50BA formulation. First, the self-assembly is triggered along θ_B=0, i.e., the horizontal direction, Figure S1d. Then, to mimic the spatial orientation of the microstructure during the printing process, the magnetic field is rotated by $\theta_B = 30°$, Figure S1e. In both cases, the numerical simulations correctly describe the dynamic evolution of the chains. After preliminary investigations on microscope slides, the formulations were tested for additive process on the modified DLP 3D printer. The necessary condition for obtaining objects with uniform magnetic properties is that the distribution of magnetic fillers inside the resin vat remains homogeneous throughout the printing process. Thus, the applied magnetic field has been first mapped by measuring its value in 13 different zones of the printing area as shown in Figure 1b. Then, the stability of the NPs distribution was tested for at least 30 min, a time compatible with the duration of the fabrication of a 5 mm thick object. Configurations composed of A-A and AA-AA magnets produce quasi-homogeneous magnetic

field distributions with an intensity at the center of the printing area of 5 mT and 10 mT, respectively, and a gradient of about $\delta Gx \approx 1 \div 2$ mT.cm^{-1} (Figure 1c,d). In both cases, a homogeneous distribution of the NPs within the printing area is observed as shown in Fig. 1e. In contrast, for the B-B, BB-BB and BA-AB configurations (Figs 1f-h) - producing a magnetic field at the center of the printing area of 11 mT, 20 mT and 15 mT, respectively, and a field gradient of about $\delta Gx \approx 5 \div 10$ mT.cm^{-1} - the migration of the fillers toward the edges of the ball bearing as well as the formation of a depleted central zone are observed, Fig. 1i. As the depletion process is driven by the gradient of the magnetic field [85], a value of $\delta Gx \approx 1 \div 2$ mT.cm^{-1} has been chosen as the upper threshold guaranteeing the homogeneous spatial distribution of the fillers during the printing step. In particular, the AA-AA configuration gives the optimum conditions to print magneto-responsive elements containing homogeneously distributed spatially oriented microstructures.

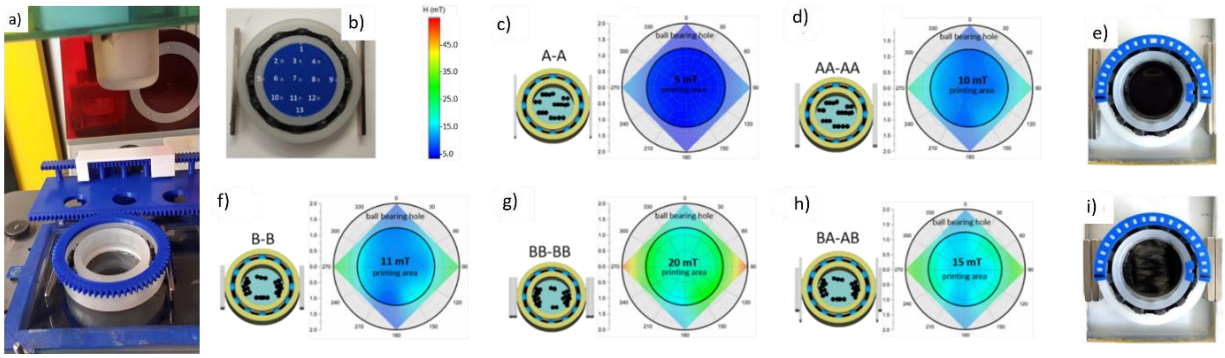

Figure 1. a) Modified DLP printer. b) Experimental mapping of the magnetic field distribution within the vat for several combinations of permanent magnets, named as A and B. A magnets are 60x10x2 mm^3 parallelepipeds exhibiting a magnetic field at the surface of 120 mT, while B magnets are 40x10x4 mm^3 parallelepipeds exhibiting a magnetic field at the surface of 310 mT. c) A-A and d) AA-AA configurations present e) a homogeneous distribution of the magnetic fillers dispersed within the photocurable resin. In contrast, for f) B-B, g) BB-BB and h) BA-AB configurations, i) inhomogeneities as well as depleted areas are observed in the vat.

The next step was the optimization of the processing parameters, for the used formulations, Table 1. As expected, the curing time (i.e., the time necessary to cure a single layer) increases with the NPs concentration, while it is only slightly influenced by the concentration of BA [76]. On the other hand, the printing parameters are not modified by the applied magnetic field used to create the microstructure.

Field Emission Scanning Electron Microscopy (FESEM) was used to verify both the efficiency of the self-assembly process during the 3D printing phase and the incorporation of the magnetic chains within the polymer matrix. Figures 2a1-c1 show that chains of magnetic fillers are

systematically observed in each prepared sample. In addition, not only their length but also their width increases with the volume fraction of the embedded NPs with a subsequent effect on the aspect ratio of the chains. These results are confirmed by the numerical simulations (Figs 2a2-c2) and can be easily understood by considering that the inter-particle distance decreases with increasing their load [86]. Thus, NPs are more likely to interact and yield larger assembled structures in highly-loaded systems than in dilute ones.

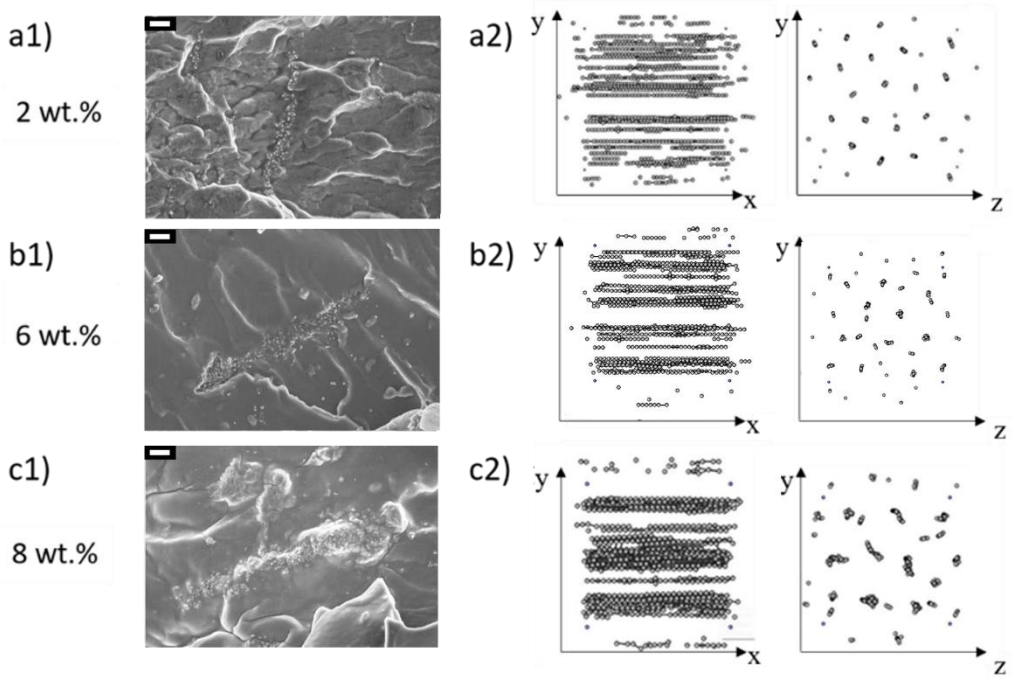

Figure 2. FESEM images of cryo-fractured 3D printed 75Eb25BA samples for increasing load of magnetic fillers: a1) 0.2 wt.%, b1) 6 wt.%, c1) 8 wt.%. The scale bar is 20 μm. a2-c2) Numerical simulations based on a dipolar approximation model.

Finally, the printability of complex objects as well as the fidelity to the original CAD file have been validated for the 75Eb25BA and 50Eb50BA formulations containing 6 wt.% of magnetic fillers, by printing an Archimede's screw containing a microstructure spatially oriented by rotating the applied magnetic field (10 mT) by θ_B=30° every 20 printed layers, i.e., 400 μm of the printed object (Fig. 3). In Fig. 3, the original STL file (Fig. 3a) and the printed object (Fig. 3b) are shown together with a heat map (Fig. 3c) reporting the differences between the digital file and the digitalization of the real object created by 3D scanning. As can be observed, the fidelity is very good (standard deviation 0.022 μm, average error about 100 μm).

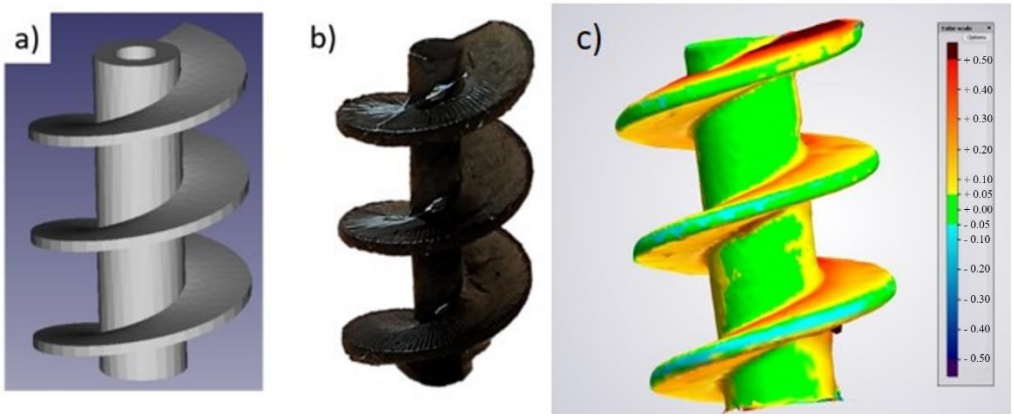

Figure 3. a) CAD file of an Archimede's screw used to check the feasibility and the fidelity of the printing process. b) Image of the printed containing a spatially oriented microstructure. c) Heat map reporting the differences between the original stl file and the digitalization of the 3D printed object obtained by 3D scanning.

The magnetic properties of a 3D printed objet containing an oriented microstructure were investigate on a 3x3x3 mm cubic specimen, as reported in Fig. 4a. The magnetic behavior of the sample containing 6 wt.% of Fe_3O_4 NPs (shown in Figure 4 b-e) is representative of all the synthetized composites loaded with different NPs concentrations. Figure 4b shows the sample containing a random dispersion of magnetic fillers. It is characterized by a perfect overlap of the hysteresis loops measured along the x, y and z axes, which in turn results in an isotropic magnetic behavior along these three equivalent directions of symmetry. In particular, the magnetization curves display the same hysteretic and reversal behavior with coercive field ($\mu_0 H_c$) of $\approx$ 12.8 mT and normalized remanent magnetization ($M_r/M_{1.5T}$) of ≈ 0.12. Conversely, the presence of chain-like structures makes the magnetic response of the printed cube anisotropic, i.e., the magnetic properties depend on the relative direction of the applied magnetic field with respect to the major axis of the chains, see Figs 4c-e. In particular, when the magnetic field is applied along the major axis of the chains (i.e., the magnetic easy axis) - black curve in Fig 4c for the chains aligned along the x-direction and red curve in Fig 4d for the chains aligned along the y-direction - the hysteresis loops appear steeper with a faster approach to saturation than those obtained by the magnetic field applied in the other directions (i.e., magnetic hard axes). Instead, for the sample where the chains are at 45°, Fig. 4e, the hysteresis loops measured along the x and y directions are now superimposed since, in this case, they are equivalent directions of symmetry with respect to the major axis of the chains. Of course, the magnetic response measured along these two equivalent directions is intermediate with respect to the ones measured along the magnetic easy and hard axes. The z-direction corresponds to the only magnetic hard axis, as confirmed by the slower approach to magnetic

saturation. In all samples, as expected, a reduction of the H_c and $M_r/M_{1.5T}$ values occurs from the easy axis to the hard one, insets in Figs 4c-e.

Cylindrical specimens with randomly distributed or oriented NPs were produced with the modified DLP 3D printer (example in Fig. 4f). The polar plot of $M_{\perp}$ measured for both randomly distributed (black curve) and self-assembled NPs (red curve) is reported in in Fig. 4g, showing the symmetry of the magnetic anisotropy induced by the microstructure of the magnetic filler. The approximately round shape of the black curve indicates an almost perfectly isotropic magnetic behavior for the sample containing randomly distributed NPs. Conversely, a two-lobes profile is observed in the sample containing magnetic chains (red curve), which is the fingerprint of the presence of a uniaxial anisotropy within the sample,[87] i.e., only one easy axis of magnetization originates from the elongated shape of the magnetic chains.

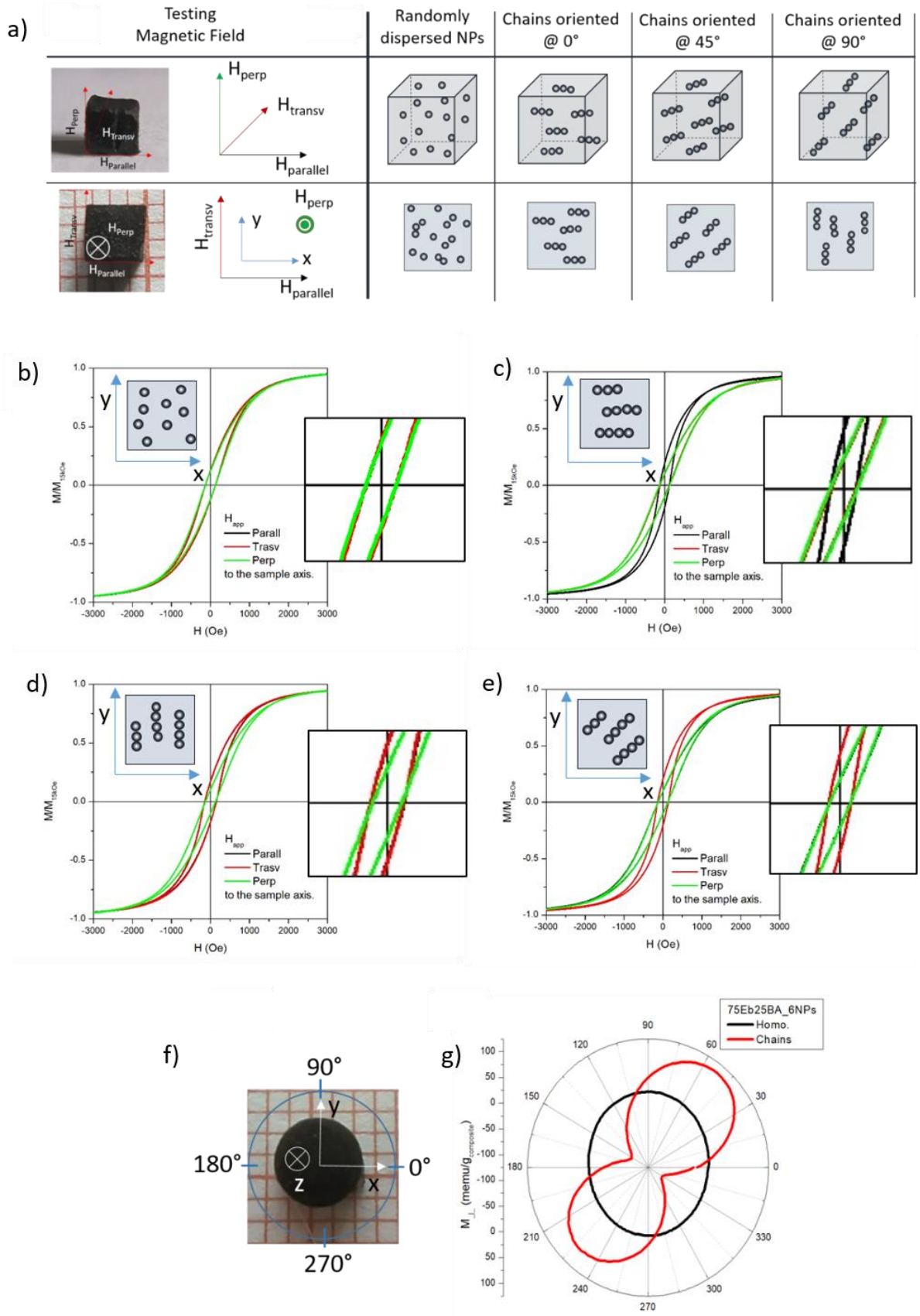

Figure 4. a) Sketch of configuration used to measure the magnetic response of a 3D printed cube. Two configurations have been probed: randomly dispersed NPs, and chains of NPs aligned along x-direction (0°), y-

direction (90°) and at 45°. Magnetic hysteresis loops measured along the x (black line), y (red line) and z (green line) directions for the 75Eb25BA_6NPs samples differing by their microstructure: b) randomly dispersed NPs, c) chains oriented at 0°, d) chains oriented at 90°, e) chains oriented at 45° with respect to the x-direction. f) 3D printed cylinder used to measure the angular dependence of the magnetic anisotropy. g) Polar plots for the perpendicular (M⊥) component of the magnetization; black curve: Fe_3O_4 nanoparticles homogenously distributed; red curve: Fe_3O_4 nanoparticles self-assembled into a chain structure. Direction is approximately 50°.

Using the magnetic susceptibility at the coercive field (χ_c) as a probing parameter, it is possible determine the amount of magnetic fillers in the printed objects that maximizes the anisotropic magnetic response. The χ_c values measured both parallel (full squares) and perpendicular (open circles) to the chains' major axis from the corresponding hysteresis loops are shown in Figure S2. The value of χ_c corresponding to the randomly distributed NPs (gray dashed line) is used as reference. As expected, for all the concentrations of NPs up to 8 wt.%, the parallel-χ_c values are systematically higher than the corresponding perpendicular-χ_c values indicating a magnetic anisotropic effect. However, the parallel-χ_c shows a non-monotonic behavior, where an increase as a function of the concentration of magnetic NPs is observed up to 4 wt.% at which a value of about 20 T^{-1} is reached. This value remains almost constant up to 6 wt.%, and then decreases at 8 wt.% to a value close to the one obtained for samples loaded with 0.5 wt.% of NPs. On the other hand, the perpendicular-χ_c values remain almost constant at about 8.5 T^{-1} close to the reference value (gray dashed line) regardless of the concentration of fillers. Thus, two conclusions can be drawn: i) the magnitude of magnetic susceptibility in the direction of the magnetic anisotropy can be tuned by the amount of NPs loaded in the polymer, with an optimum concentration of the fillers in the range 4-6 wt.%; ii) along the direction perpendicular to the chains' major axis, the effect of the anisotropy is weak. Moreover, the magnitude of the magnetic susceptibility in the directions perpendicular to the easy axis is almost independent on the NPs concentration as it is observed that the magnetization reversal mechanism is very similar to that of uniformly dispersed NPs.

An estimate of the average chains' aspect ratio (α) and of the contribution to the effective magnetic anisotropy by the chain shape (K_s) has been obtained by using the procedure described in the SI and is reported in Figure S3c for all Fe_3O_4-loaded printed samples. The value of α shows a non-monotonic behavior with a maximum value of about 1.8 for a NP concentration in the range 4-6 wt.%. This suggests that an initial increase in NP concentration within the polymer composite leads to the formation of longer chains, in agreement with SEM observations and numerical simulations (see Fig. 2) as well as existing literature [61,88,89]. On the other hand, the reduced value of α observed for a load of 8 wt.% can be explained by the fact that when the

amount of embedded NPs overcomes a threshold value, the self-assembly process forms overlapping and interconnected magnetic chains (see Fig.2c2). Therefore, the chains no longer act as isolated magnetic units but as larger and interacting magnetic assemblies. This affects the overall magnetic behavior by reducing the contribution to the effective magnetic anisotropy, and in turn by decreasing the magnetic susceptibility of the composite material. In addition, the evolution of K_s values, also shown in Figure S3c, has a similar trend to that of α with a maximum value of about $6.3x10^3$ J/m^3 in the range 4-6 wt.% of embedded NPs, which thus represents the optimum load of magnetic fillers. These results show the effectiveness of the magnetic field-driven self-assembly process during the DLP printing step to program the effective magnetic anisotropy of the polymer composite, which in turn induces a net magnetic moment capable of yielding an actuation motion by magnetic torque.

We previously demonstrated [76] that the stiffness of the printed composite can be tuned by varying the amount of butyl-acrylate (BA) in the Ebecryl (Eb) resin, and that the optimum concentration of fillers for the printing process under the application of a constant magnetic field of 10 mT is 6 wt.%. Here, the effect of the orientation of the chains on the mechanical properties of the printed materials was studied (Figure S4). For the stiffer sample (75Eb25BA_6NPs), the value of the elastic modulus is, within the error bar, equivalent to that of the reference sample, i.e., E~4.5 MPa. Thus, the orientation of the microstructure does not alter the mechanical response of the composites when subjected to tensile stress. For the softer sample (50Eb50BA_6NPs), a reduction of the elastic modulus of about 10 % is observed with respect to the reference sample containing only dispersed NPs, i.e., E~3.75 MPa. This is presumably due to the incorporation of larger aggregate-inducing defects, as already observed in soft samples [76].

Once both the magnetic and mechanical properties of the 3D printed materials with oriented nanoparticles were studied in detail, the information was subsequently employed to develop 3D printed objects with programmed response, and finally 3D printed magnetic devices, exploiting magnetic fields. Indeed, when a 3D printed devices containing a magnetic microstructure is subjected to an external magnetic field, a magnetic torque (τ_m) is exerted on the extended magnetic dipole, which forces the chains to rotate in order to align their easy magnetic axis along the field direction [64,69,90–94]. In general, the magnetic torque can be expressed as: $\tau_m = dU_m/d\theta$, where U_m is the magnetic energy of the material and θ is the rotation angle. Approximating a chain to a prolate ellipsoid with a and b its long and short dimensions, U_m can be written as [64]:

$$U_m = \frac{2\pi ab^2}{3}\frac{\bar{\chi}^2}{\bar{\chi}+2}\mu_0 H^2 \sin^2\theta \quad (1)$$

where $\bar{\chi} = 3\chi/\chi + 2$ is the shape-corrected susceptibility of the magnetic unit and H is the applied magnetic field. When the magnetic chains are confined within and anchored to the host polymeric matrix, the torque is transferred to the whole material. In this case, two pathways are possible: if the composite is rigid it will be subject to an overall rotation; conversely, if the composite is soft and the magnetic torque overcomes the mechanical resistance of the material, the object will deform [64,69,94]. Thus, using the modified DLP printer to control of the microstructure during the printing process, as well as the initial formulation to tune the stiffness of the printed sample, several magnetically-driven actuators have been obtained.

First, rigid hammer-like structures undergoing predefined rotations were obtained. The magneto-responsive hammers were 3D printed using the 75Eb25BA formulation loaded with 6 wt.% of NPs, 75Eb25BA_6NPs (Fig. 5a). Five hammers were printed, each having a defined orientation of the microstructure, i.e., 0°, 45°, 90°, 135°, and 180° as indicated by the arrows in Fig. 5b. To minimize the friction effects, the hammers were placed in a petri dish filled with water and each hammer was anchored to a pinion of a 3D printed rack. Their rotations were studied by using a pair of Helmholtz coils generating a magnetic field up to 4 mT in the x-y plane, Figure S5 in SI.

In the initial configuration, the magnetic field is switched off (H=0) and all the hammers are parallel one to another as shown in Fig. 5c. As soon as the field is applied (H=+4 mT) in the direction indicated in Fig. 5d, each hammer starts to rotate around its anchoring point until the equilibrium configuration is reached, Fig. 5e. This is until the microstructure, indicated by the arrow, aligns to the direction of the applied field. As each hammer has a specific microstructure, they rotate at a different angle. By reversing the direction of the applied field (H=-4 mT), it is possible to reverse the process, Fig. 5f. Finally, the repeatability of the process is demonstrated by inverting again the direction of the applied field (H=+4 mT), Figs. 5g-h. A complete sequence of the controlled motion of these actuators is reported in video S1.

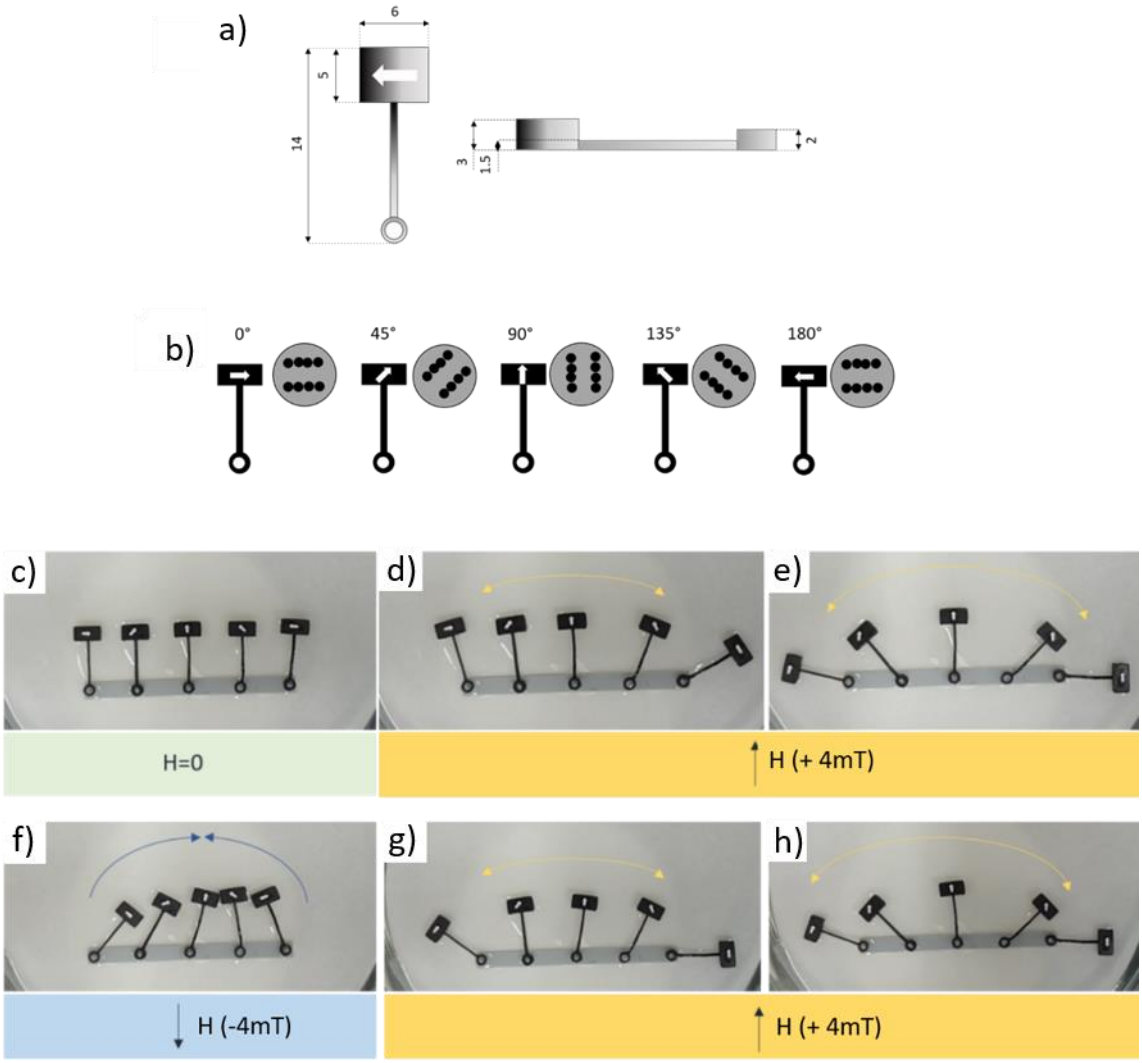

Figure 5. a) Dimensions of the 3D printed rigid magnetic hammers (mm) and b) orientation of the microstructure within each hammer. c-h) Time evolution of rigid magneto-responsive hammers having different orientations of the microstructure (indicated by the arrows) as a function of the applied magnetic field.

A similar approach was then used to exploit the bending of printed soft composites. In this case, the magnetic force (τ_{Magnetic}) must overcome the mechanical resistance of the material (τ_{Mechanic}) to obtain bending. Thus, magneto-responsive flexible actuators can be printed by either increasing the intensity of the applied magnetic field or by reducing the mechanical resistance of the sample. The latter option can be obtained either by tuning the stiffness of the matrix and/or by changing the geometry of the sample. In the present case, both the mechanical properties of the object and its design have been adapted. In particular, a soft hammer was printed using the 50Eb50BA formulation loaded with 6 wt.% of NPs (50Eb50BA_6NPs) and its mechanical resistance was decreased by locally reducing the thickness of the hammer's arm as indicated in Fig. 6a. Again, he friction effects have been minimized by placing the hammer

in a petri dish filled with water. Contrarily to the rigid hammers, the extremity of the flexible hammer was fixed to a support for preventing the object to rotate. As the bending of a millimeter-size actuator necessitates an intensity of the magnetic field larger than the one that can be obtained using standard Helmholtz coils, a couple of NdFeB permanent magnets have been used to activate the actuation process as described in SI. The initial configuration (H=0) is shown in Fig. 6b, where the orientation of the microstructure is indicated by the arrow. A magnetic field is then applied normally to the microstructure, whose magnitude was tuned by an Arduino controller by varying the relative distance between a couple of magnets. Below a critical distance the magnetic torque (τ_{mag}) overcomes the mechanical one (τ_{mech}) and the hammer starts bending to re-align its easy magnetic axis in the direction of the field, Fig. 6c. As expected, when reversing the polarity of the magnets, the bending is observed in the opposite direction, Fig 6d. The complete sequence of the bending of the hammer is reported in video S2.

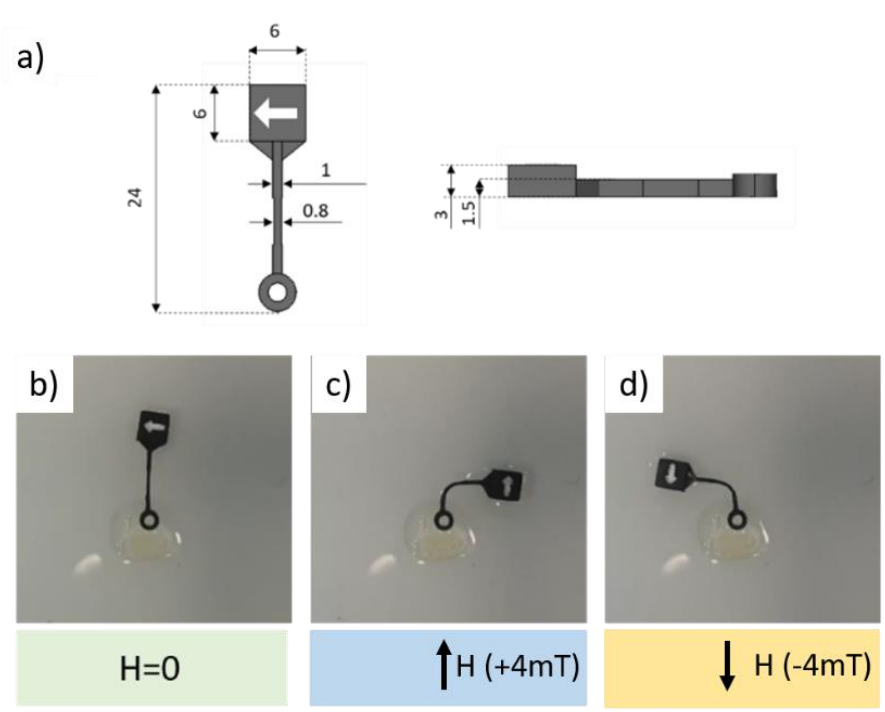

Figure 6: a) Design of a magneto-responsive soft hammer. The microstructure is indicated by the arrow on the head of the hammer. b) Initial configuration (H=0) and c)-b) bending of the of magneto-responsive soft hammer for two opposite directions of the applied magnetic field.

To increase the degree of complexity on our objects we checked the possibility to 3D print magnetically-driven gears. Mechanical gears are toothed wheels that transmit rotation and power from one shaft to another, or that work in combination with one or more other gears to alter the relationship between the speeds of the driver and the driven parts. Magnetic gears, first

patented by Armstrong in 1901 [95], resemble the traditional mechanical gears in geometry and function, except that the force/torque transmission exerted by tooth meshing is replaced with the contactless magnetic interaction. As two opposing magnets approach each other, they repel; when placed on two rings the magnets will act like teeth.

First, the feasibility of remote control of gear rotation has been verified by printing two identical elements, i.e., using the same formulation (75Eb25BA_6NPs) and the same design (10 teeth, 1 mm module, and a pressure angle of 20°), but with different microstructures (oriented and dispersed NPs) as reported in Fig. S6. The reversibility of the process has been checked by switching the magnetic field several times. The complete sequence is reported in Fig. S6 and in video S3. The interpretation of these experimental results is quite straightforward, and it is clearly related to the different microstructures of the two objects. On one hand, a sample containing dispersed NPs is magnetically isotropic as indicated by the hysteresis cycles (Fig. 4b), thus the application of a uniform magnetic field does not generate a net magnetic torque, and the rotation of the sample is nearly absent. On the other hand, the presence of a microstructure in the sample creates a magnetic anisotropy in the object, which in turn generates a magnetic torque ($\sim M_{easy} \times H$) forcing the gear to rotate.

When two or more gears are linked together, the ensemble is considered as a gear train where the "input gear" (also known as drive gear) transmits the power to the "output gear" (also known as driven gear), Fig. S7. In a standard gear train, the input gear is typically connected to a power source, such as a DC motor. In this case, the magneto-active drive gear is remotely controlled by an external magnetic field, and the driven gear is non-magnetic and printed using an inert resin. The complete sequence of work is reported in the Supporting Information of this manuscript (Fig S7 and Video S4).

A further step was to fabricate a linear actuator composed of a spur gear and a linear rack coupled together through the meshing of their respective teeth. The complete sequence as well as the explanation of the process is reported in the Supporting Information of this manuscript (Fig. S8 Video S5).

The linear actuator was then employed to build a magnetic driven gripper. Generally speaking, grasping is the ability to pick up and hold an object, while manipulation is the ability to produce rotation and displacement. Grasping and manipulation are two functions that are of paramount importance in robotics as they allow the machine to mimic the behavior of human beings and animals. This device is composed of two non-magnetic clamping arms activated by a magneto-responsive linear actuator. In the literature, some magnetically-driven gripper have been reported, but they are based on the 3D printing of magnetic composites [96,97]. In contrast, in the

present case, the magnetic component was decoupled from the gripping part, allowing remote control without the necessity to insert magnets close to the gripping part, but instead exploiting the programmed microstructure of the gears. The operation of this magneto-responsive gripper is illustrated in Fig. 8a-g. In the initial configuration, the two arms of the grippers are in the open position, i.e., they are far from each other. When the magnetic field is switched on, the magneto-responsive drive gear stars to rotate anti-clockwise, transferring its motion to the rack. Then, a couple of driven gears transform again the translating motion of the rack into a rotary one. As they have been printed with an arm and a clamp, they play the role of the hands of the gripper. Inverting the field allows the magneto-responsive spur gear to rotate clockwise, and the arms of the gripper to open up and return to their initial configuration. The complete sequence is reported in the Supporting Information of this manuscript (Video S6). This proof-of-concept example indicates that the development of magneto-responsive devices with advanced functionalities is technically possible.

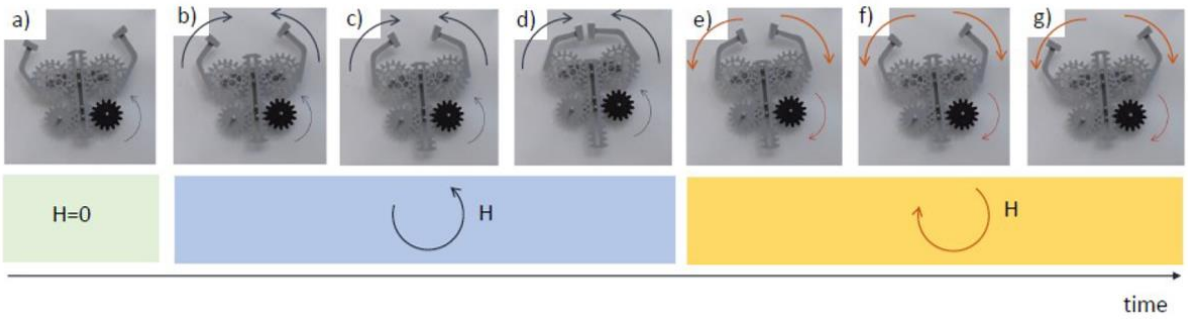

Figure 8: a-g) Timeframe evolution of the magnetically-driven clamp driven by a magneto-active drive gear.

5. Conclusion

Magneto-responsive polymers with oriented microstructures behave as magnetic compasses. Indeed, when a uniform magnetic field is applied, the composite sample undergo rotation movements (if rigid) or bending (if soft) to align its easy magnetic axis along the field lines. Taking advantage of this phenomenon, we printed magnetically-driven macroscopic elements undergoing programmed movements by the remote application of a magnetic field. Our approach is based on the ability to tune the self-assembly of the magnetic microstructure (Fe_3O_4) and to control its orientation in a photocurable resin during the printing process thanks to the modification of a DLP-type printer.

In this work, our approach is first applied to fabricate magneto-responsive hammer-like actuators with different stiffness allowing both pure rotation or/and bending motions. As

application, these elements could be used to create a magneto-responsive electric-switch. Then, by introducing the idea that the microstructure can be exploited to create a magneto-responsive gear, we showed that the latter can be successfully used to transfer torque to other gears, thereby converting a rotation movement into linear translation. Finally, we demonstrated that magneto-responsive gears can be also combined with other non-magnetic elements to create complex assemblies, such as gear-trains, linear actuators and grippers, that can be remotely controlled. We believe that our approach can be further developed to achieve even more complex component systems and could generate new opportunities in robotics-related applications.

References

[1] P. Fratzl, R. Weinkamer, *Prog. Mater. Sci.* **2007**, *52*, 1263. DOI 10.1016/j.pmatsci.2007.06.001

[2] P. Fratzl, *J. R. Soc. Interface* **2007**, *4*, 637. DOI 10.1098/RSIF.2007.0218

[3] J. C. Weaver, G. W. Milliron, A. Miserez, K. Evans-Lutterodt, S. Herrera, I. Gallana, W. J. Mershon, B. Swanson, P. Zavattieri, E. DiMasi, D. Kisailus, *Science.* **2012**, *336(6086)*, 1275-1280 DOI 10.1126/science.1218764.

[4] L. K. Grunenfelder, N. Suksangpanya, C. Salinas, G. Milliron, N. Yaraghi, S. Herrera, K. Evans-Lutterodt, S. R. Nutt, P. Zavattieri, D. Kisailus, in *Acta Biomater.*, **2014**, *10(9)*, 3997-4008**.** DOI 10.1016/j.actbio.2014.03.022.

[5] A. M. C. Emons, B. M. Mulder, *Trends Plant Sci.* **2000**, *5(1)*, 35-40 DOI 10.1016/S1360-1385(99)01507-1.

[6] I. Burgert, P. Fratzl, *Integr. Comp. Biol.* **2009**, *49(1)*, 69-79, DOI 10.1093/icb/icp026.

[7] A. Fabricant, G. Z. Iwata, S. Scherzer, L. Bougas, K. Rolfs, A. Jodko-Władzińska, J. Voigt, R. Hedrich, D. Budker, *Sci. Rep.* **2021**, *11*, 1438, DOI 10.1038/s41598-021-81114-w.

[8] R. Sachse, A. Westermeier, M. Mylo, J. Nadasdi, M. Bischoff, T. Speck, S. Poppinga, *Proc. Natl. Acad. Sci. U. S. A.* **2020**, *117(27)*, 16035-16042, DOI 10.1073/pnas.2002707117.

[9] A. Le Duigou, M. Castro, *Ind. Crops Prod.* **2017**, *99*, 142-149, DOI 10.1016/j.indcrop.2017.02.004.

[10] A. Scheffel, M. Gruska, D. Faivre, A. Linaourodis J.M. Plitzko, D. Schüler *Nature* **2006**, *440*, 110–114, DOI 10.1038/nature04382

[11] S. Tibbits, *Archit. Des.*, **2014**, *84(1)*, 116-121, DOI https://doi.org/10.1002/ad.1710**.**

[12] Z. X. Khoo, J. E. M. Teoh, Y. Liu, C. K. Chua, S. Yang, J. An, K. F. Leong, W. Y.

Yeong, *Virtual Phys. Prototyp.* **2015**, 103-122, DOI 10.1080/17452759.2015.1097054.

[13] A. Mitchell, U. Lafont, M. Hołyńska, C. Semprimoschnig, *Addit. Manuf.*, **2018**, *24*, 606-626, DOI 10.1016/j.addma.2018.10.038.

[14] D. G. Shin, T. H. Kim, D. E. Kim, *Int. J. Precis. Eng. Manuf. - Green Technol.* **2017**,*4(3)*, 349-357, DOI 10.1007/s40684-017-0040-z.

[15] S. E. Bakarich, R. Gorkin, M. In Het Panhuis, G. M. Spinks, *Macromol. Rapid Commun.* **2015**, *36(12)*, 1211-1217, DOI 10.1002/marc.201500079.

[16] Y. Hu, Z. Wang, D. Jin, C. Zhang, R. Sun, Z. Li, K. Hu, J. Ni, Z. Cai, D. Pan, X. Wang, W. Zhu, J. Li, D. Wu, L. Zhang, J. Chu, *Adv. Funct. Mater.* **2020**, *30(4)*, 1907377, DOI 10.1002/adfm.201907377.

[17] J. Guo, R. Zhang, L. Zhang, X. Cao, *ACS Macro Lett.* **2018**, *7(4)*, 442-446, DOI 10.1021/acsmacrolett.7b00957.

[18] M. N. I. Shiblee, K. Ahmed, M. Kawakami, H. Furukawa, *Adv. Mater. Technol.* **2019**, *4(8)*, 1900071, DOI 10.1002/admt.201900071.

[19] L. H. Shao, B. Zhao, Q. Zhang, Y. Xing, K. Zhang, *Extrem. Mech. Lett.* **2020**, *39*, 100793, DOI 10.1016/j.eml.2020.100793.

[20] D. Grinberg, S. Siddique, M. Q. Le, R. Liang, J. F. Capsal, P. J. Cottinet, *J. Polym. Sci. Part B Polym. Phys.* **2019**, 57(2), 109-115, DOI 10.1002/polb.24763.

[21] T. Mirfakhrai, J. D. W. Madden, R. H. Baughman, *Mater. Today* **2007**, *10(4)*, 30-38, DOI 10.1016/S1369-7021(07)70048-2.

[22] H. Meng, G. Li, *Polymer (Guildf).* **2013**, *54(9)*, 2199-2221, DOI 10.1016/j.polymer.2013.02.023.

[23] J. Wu, C. Yuan, Z. Ding, M. Isakov, Y. Mao, T. Wang, M. L. Dunn, H. J. Qi, *Sci. Rep.* **2016**, *6*, 24224, DOI 10.1038/srep24224.

[24] K. Yu, A. Ritchie, Y. Mao, M. L. Dunn, H. J. Qi, in *Procedia IUTAM*, **2015**. *12*, 193-293, DOI 10.1016/j.piutam.2014.12.021

[25] Y. Mao, K. Yu, M. S. Isakov, J. Wu, M. L. Dunn, H. Jerry Qi, *Sci. Rep.* **2015**, *5*, 13616, DOI 10.1038/srep13616.

[26] M. Zarek, M. Layani, I. Cooperstein, E. Sachyani, D. Cohn, S. Magdassi, *Adv. Mater.* **2016**, *28(22)*, 4449-4454, DOI 10.1002/adma.201503132.

[27] A. Muzaffar, M. B. Ahamed, K. Deshmukh, T. Kovářík, T. Křenek, S. K. K. Pasha, in *3D 4D Print. Polym. Nanocomposite Mater. Process. Appl. Challenges*, **2019**. 85-117, DOI 10.1016/B978-0-12-816805-9.00004-1

[28] X. Zhang, P. Yang, Y. Dai, P. Ma, X. Li, Z. Cheng, Z. Hou, X. Kang, C. Li, J. Lin,

Adv. Funct. Mater. **2013**, *23*, 4067-4078, DOI 10.1002/adfm.201300136.

[29] H. Yang, W. R. Leow, T. Wang, J. Wang, J. Yu, K. He, D. Qi, C. Wan, X. Chen, *Adv. Mater.* **2017**, *29(33)*, 1701627, DOI 10.1002/adma.201701627.

[30] I. Roppolo, A. Chiappone, A. Angelini, S. Stassi, F. Frascella, C. F. Pirri, C. Ricciardi, E. Descrovi, *Mater. Horizons* **2017**, *4*, 396-401, DOI 10.1039/c7mh00072c.

[31] L. Ren, X. Zhou, Q. Liu, Y. Liang, Z. Song, B. Zhang, B. Li, *J. Mater. Sci.* **2018**, *53(20)*, 14274-14286, DOI 10.1007/s10853-018-2447-5.

[32] J. J. Martin, B. E. Fiore, R. M. Erb, *Nat. Commun.* **2015**, *6*, 8641,DOI 10.1038/ncomms9641.

[33] Z. Jia, Y. Yu, S. Hou, L. Wang, *J. Mech. Phys. Solids* **2019**, *125*, 178-197, DOI 10.1016/j.jmps.2018.12.015.

[34] Y. Yang, X. Li, M. Chu, H. Sun, J. Jin, K. Yu, Q. Wang, Q. Zhou, Y. Chen, *Sci. Adv.* **2019**, *5(4)*, DOI 10.1126/sciadv.aau9490.

[35] B. Wang, T. N. Sullivan, A. Pissarenko, A. Zaheri, H. D. Espinosa, M. A. Meyers, *Adv. Mater.* **2019**, *31(3)*, 1804574, DOI 10.1002/adma.201804574.

[36] L. Zorzetto, D. Ruffoni, *Adv. Funct. Mater.* **2019**, *29(1)*, 1805888, DOI 10.1002/adfm.201805888.

[37] M. Peng, Z. Wen, L. Xie, J. Cheng, Z. Jia, D. Shi, H. Zeng, B. Zhao, Z. Liang, T. Li, L. Jiang, *Adv. Mater.* **2019**, *31(35)*, 1902930, DOI 10.1002/adma.201902930.

[38] S. M. Sajadi, P. S. Owuor, S. Schara, C. F. Woellner, V. Rodrigues, R. Vajtai, J. Lou, D. S. Galvão, C. S. Tiwary, P. M. Ajayan, *Adv. Mater.* **2018**, *30(1)*, 1704820, DOI 10.1002/adma.201704820.

[39] L. Ren, B. Li, Z. Song, Q. Liu, L. Ren, X. Zhou, *Int. J. Precis. Eng. Manuf. - Green Technol.* **2019**, *6*, 89-99, DOI 10.1007/s40684-019-00030-7.

[40] J. R. Raney, B. G. Compton, J. Mueller, T. J. Ober, K. Shea, J. A. Lewis, *Proc. Natl. Acad. Sci. U. S. A.* **2018**, *115(6)*, 1198-1203, DOI 10.1073/pnas.1715157115.

[41] H. Arslan, A. Nojoomi, J. Jeon, K. Yum, *Adv. Sci.* **2019**, *6(2)*, 1800703, DOI 10.1002/advs.201800703.

[42] J. Liu, O. Erol, A. Pantula, W. Liu, Z. Jiang, K. Kobayashi, D. Chatterjee, N. Hibino, L. H. Romer, S. H. Kang, T. D. Nguyen, D. H. Gracias, *ACS Appl. Mater. Interfaces* **2019**, *11(8)*, 8492-8494, DOI 10.1021/acsami.8b17218.

[43] A. Nojoomi, H. Arslan, K. Lee, K. Yum, *Nat. Commun.* **2018**, *9*, 3705, DOI 10.1038/s41467-018-05569-8.

[44] M. Schaffner, J. A. Faber, L. Pianegonda, P. A. Rühs, F. Coulter, A. R. Studart, *Nat.*

Commun. **2018**, *9*, 878, DOI 10.1038/s41467-018-03216-w.

[45] Y. Hu, A. Xu, J. Liu, L. Yang, L. Chang, M. Huang, W. Gu, G. Wu, P. Lu, W. Chen, Y. Wu, *Adv. Mater. Technol.* **2019**, *4(3)*, 1800674, DOI 10.1002/admt.201800674.

[46] S. Ma, M. Scaraggi, C. Yan, X. Wang, S. N. Gorb, D. Dini, F. Zhou, *Small* **2019**, 4(3), 1800674, DOI 10.1002/smll.201802931 [47]N. Bira, P. Dhagat, J. R. Davidson, *Front. Robot. AI* **2020**, *7*, 146.

[48] K. J. Merazzo, A. C. Lima, M. Rincó N-Iglesias, L. C. Fernandes, N. Pereira, S. Lanceros-Mendez, P. Martins, *Mater. Horiz* **2021**, *8*, 2654 DOI 10.1039/d1mh00641j.

[49] S. Malley, S. Newacheck, G. Youssef, *Addit. Manuf.* **2021**, *47*, 102239, DOI https://doi.org/10.1016/j.addma.2021.102239

[50] F. Qiu, B. J. Nelson, *Engineering* **2015**, *1(1)*, 21-26, DOI 10.15302/J-ENG-2015005.

[51] H. Ceylan, J. Giltinan, K. Kozielski, M. Sitti, *Lab Chip* **2017**, *17*, 1705-1724, DOI 10.1039/c7lc00064b.

[52] B. Nagarajan, P. Mertiny, A. J. Qureshi, *Mater. Today Commun.* **2020**, *25*, 101520, DOI 10.1016/j.mtcomm.2020.101520.

[53] Y. Zhang, Q. Wang, S. Yi, Z. Lin, C. Wang, Z. Chen, L. Jiang, *ACS Appl. Mater. Interfaces* **2021**, *13(3)*, 4174-4184, DOI 10.1021/acsami.0c19280.

[54] S. Lucarini, M. Hossain, D. Garcia-Gonzalez, *Compos. Struct.* **2022**, *279*, 114800, DOI 10.1016/j.compstruct.2021.114800.

[55] Y. Kim, H. Yuk, R. Zhao, S. A. Chester, X. Zhao, *Nature* **2018**, *558*, 274-279, DOI 10.1038/s41586-018-0185-0.

[56] M. Xie, W. Zhang, C. Fan, C. Wu, Q. Feng, J. Wu, Y. Li, R. Gao, Z. Li, Q. Wang, Y. Cheng, B. He, *Adv. Mater.* **2020**, *32*, 2000366. DOI 10.1002/adma.202000366

[57] H. Song, H. Lee, J. Lee, J. K. Choe, S. Lee, J. Y. Yi, S. Park, J.-W. Yoo, M. S. Kwon, J. Kim, *Nano Lett.* **2020**, *20*, 5185-5192, DOI 10.1021/acs.nanolett.0c01418.

[58] J. Zhang, Y. Wang, H. Pang, S. Sun, Z. Xu, L. Shen, X. Cao, C. Sun, B. Wang, X. Gong, *Compos. Part A Appl. Sci. Manuf.* **2021**, *150*, 106591, DOI 10.1016/j.compositesa.2021.106591.

[59] A. A. Kuznetsov, *J. Magn. Magn. Mater.* **2019**, *470*, 28-32, DOI 10.1016/j.jmmm.2017.10.091.

[60] W. Zhang, P. K. J. Wong, D. Zhang, J. Yue, Z. Kou, G. van der Laan, A. Scholl, J. G. Zheng, Z. Lu, Y. Zhai, *Adv. Funct. Mater.* **2017**, 27(29), 1701265, DOI 10.1002/adfm.201701265.

[61] Y. Zhang, L. Sun, Y. Fu, Z. C. Huang, X. J. Bai, Y. Zhai, J. Du, H. R. Zhai, *J. Phys.*

Chem. C **2009**, *113(19)*, 8152-8157, DOI 10.1021/jp807937d.

[62] Y. I. Dikansky, D. V. Gladkikh, A. A. Zakinyan, A. G. Ispiryan, A. R. Zakinyan, *J. Mol. Liq.* **2020**, *319*, 114171, DOI 10.1016/j.molliq.2020.114171.

[63] D. Lisjak, A. Mertelj, *Prog. Mater. Sci.* **2018**, *95*, 286-328, DOI 10.1016/j.pmatsci.2018.03.003.

[64] R. M. Erb, J. J. Martin, R. Soheilian, C. Pan, J. R. Barber, *Adv. Funct. Mater.* **2016**, *26(22)*, 3859-3880, DOI 10.1002/adfm.201504699.

[65] L. Zhang, J. J. Abbott, L. Dong, B. E. Kratochvil, D. Bell, B. J. Nelson, *Appl. Phys. Lett.* **2009**, *94*, 064107, DOI 10.1063/1.3079655.

[66] R. M. Erb, J. S. Sander, R. Grisch, A. R. Studart, *Nat. Commun.* **2013**, *4*, 1712, DOI 10.1038/ncomms2666.

[67] S. R. Mishra, M. D. Dickey, O. D. Velev, J. B. Tracy, *Nanoscale* **2016**, *8*, 1309-1313, DOI 10.1039/c5nr07410j.

[68] A. Crivaro, R. Sheridan, M. Frecker, T. W. Simpson, P. Von Lockette, *J. Intell. Mater. Syst. Struct.* **2016**, 1-13, DOI 10.1177/1045389X15620037.

[69] J. Kim, S. E. Chung, S. E. Choi, H. Lee, J. Kim, S. Kwon, *Nat. Mater.* **2011**, *10*, 747-752,DOI 10.1038/nmat3090.

[70] H. Ceylan, I. C. Yasa, O. Yasa, A. F. Tabak, J. Giltinan, M. Sitti, *ACS Nano* **2019**, *13(3)*, 3353-3362, DOI 10.1021/acsnano.8b09233.

[71] C. Peters, O. Ergeneman, P. D. W. García, M. Müller, S. Pané, B. J. Nelson, C. Hierold, *Adv. Funct. Mater.* **2014**, *24(33)*, 5269-5276, DOI 10.1002/adfm.201400596.

[72] Y. W. Lee, H. Ceylan, I. C. Yasa, U. Kilic, M. Sitti, *ACS Appl. Mater. Interfaces* **2021**, *13(11)*, 12759-12766, DOI 10.1021/acsami.0c18221.

[73] H. C. M. Sun, P. Liao, T. Wei, L. Zhang, D. Sun, *Micromachines* **2020**, *11(4)*, 404, DOI 10.3390/MI11040404.

[74] J. Giltinan, V. Sridhar, U. Bozuyuk, D. Sheehan, M. Sitti, *Adv. Intell. Syst.* **2021**, *3(1)*, 2000204, DOI 10.1002/aisy.202000204.

[75] R. Tognato, A. R. Armiento, V. Bonfrate, R. Levato, J. Malda, M. Alini, D. Eglin, G. Giancane, T. Serra, *Adv. Funct. Mater.* **2019**, *29(9)*, 1804647, DOI 10.1002/adfm.201804647.

[76] S. Lantean, G. Barrera, C. F. Pirri, P. Tiberto, M. Sangermano, I. Roppolo, G. Rizza, *Adv. Mater. Technol.* **2019**, *29(9)*, 1804647, DOI 10.1002/admt.201900505.

[77] S. Lantean, I. Roppolo, M. Sangermano, M. Hayoun, H. Dammak, G. Rizza, *Addit. Manuf.* **2021**, *47*, 102343, DOI 10.1016/J.ADDMA.2021.102343.

[78] C. H. Bennett, in *Diffus. Solids*, **1975**. DOI 10.1016/b978-0-12-522660-8.50007-6.

[79] J. R. Beeler, Jr, R. E. Dahl, Jr, R. D. Bourquin, *Le J. Phys. Colloq.* **1975**, DOI 10.1051/jphyscol:1975411.

[80] I. S. Novikau, P. A. Sánchez, S. S. Kantorovich, *J. Mol. Liq.* **2020**, 307, 112902, DOI 10.1016/j.molliq.2020.112902.

[81] Y. Men, W. Wang, P. Xiao, J. G Y. Men, W. Wang, P. Xiao, J. Gu, A. Sun, Y. Huang, J. Zhang, T. Chen, *RSC Adv.* **2015**, *5*, 31519-31524, DOI 10.1039/c5ra02160j.

[82] B. M. Smirnov, E. E. Son, D. V Tereshonok, *J. Exp. Theor. Phys.* **2017**, *125*, 906. DOI 10.1134/S1063776117110073.

[83] M. A. M. Gijs, *Microfluid. Nanofluidics* **2004**, *1*, 22-40, DOI 10.1007/s10404-004-0010-y.

[84] N. Pamme, *Lab Chip* **2006**, *6*, 24-38, DOI 10.1039/b513005k.

[85] N. A. Spaldin, *Magnetic Materials: Fundamentals and Applications*, **2010**. DOI 10.1017/CBO9780511781599

[86] V. S. Andreev, A. E. Luk'yanov, *Colloid J. USSR* **1990**, *51*, 643-645.

[87] Q. Wu, W. He, H.L. Liu, J. Ye, X.Q. Zhang, H.T. Yang, Z.Y Chen, Z.H Cheng *Sci. Rep.* **2013**, *3*,1547, DOI 10.1038/srep01547

[88] M. Varón, M. Beleggia, T. Kasama, R. J. Harrison, R. E. Dunin-Borkowski, V. F. Puntes, C. Frandsen, *Sci. Rep.* **2013**, *3*, 1234, DOI 10.1038/srep01234.

[89] B. D. Cullity, C. D. Graham, *Introduction to Magnetic Materials*, **2008**. DOI 10.1002/9780470386323.

[90] Z. Li, F. Yang, Y. Yin, *Adv. Funct. Mater.* **2020**, *30(2)*, 1903467, DOI 10.1002/adfm.201903467.

[91] P. Von Lockette, in *ASME 2014 Conf. Smart Mater. Adapt. Struct. Intell. Syst. SMASIS 2014*, **2014**. DOI 10.1115/SMASIS20147590

[92] H. W. Huang, M. S. Sakar, A. J. Petruska, S. Pané, B. J. Nelson, *Nat. Commun. 7*, 12263, **2016**, DOI 10.1038/ncomms12263.

[93] T. Li, J. Li, K. I. Morozov, Z. Wu, T. Xu, I. Rozen, A. M. Leshansky, L. Li, J. Wang, *Nano Lett.* **2017**, *17(8)*, 5092-5098, DOI 10.1021/acs.nanolett.7b02383.

[94] L. Bodelot, J. P. Voropaieff, T. Pössinger, *Exp. Mech.* **2018**, *58*, 207. DOI 10.1007/S11340-017-0334-7

[95] C.G. Armstrong, **1900,** US671330A.

[96] Z. Ji, C. Yan, B. Yu, X. Wang, F. Zhou, *Adv. Mater. Interfaces* **2017**, *4(22)*, 1700629, DOI 10.1002/admi.201700629.

[97] X. Cao, S. Xuan, S. Sun, Z. Xu, J. Li, X. Gong, *ACS Appl. Mater. Interfaces* **2021**, *13*, 30136. DOI 10.1021/acsami.1c08252

Adv. Mater. Technol. **2022**, 2200288 **DOI: 10.1002/admt.202200288**

Supplementary Information

Magnetoresponsive Devices with Programmable Behavior Using a Customized Commercial Stereolithographic 3D Printer

Simone Lantean [1,2], Ignazio Roppolo [1,3*], Marco Sangermano[1], Marc Hayoun[2], Hichem Dammak [2,4], Gabriele Barrera[5], Paola Tiberto[5], Laurence Bodelot[6], Giancarlo Rizza[2]

1. Department of Applied Science and Technology, Politecnico di Torino, Duca degli Abruzzi, 24, 10124, Torino, Italy
2. Laboratoire des Solides Irradiés (LSI), Institut Polytechnique de Paris, CEA/DRF/IRAMIS, CNRS, Ecole polytechnique, Route de Saclay, 91128 Palaiseau, France
3. Center for Sustainable Future Technologies, Istituto Italiano di Tecnologia, Via Livorno 60, 10144, Torino, Italy
4. Laboratoire Structures Propriétés et Modélisation des Solides, CentraleSupélec, CNRS, Université Paris-Saclay, F 91190 Gif-sur-Yvette, France
5. Advanced Materials for Metrology and Life Sciences Division INRiM Strada delle Cacce 91, 10143 Torino, Italy
6. Laboratoire de Mécanique des Solides (LMS), CNRS, École polytechnique, Institut Polytechnique de Paris, Route de Saclay, 91128 Palaiseau, France

E-mail: ignazio.roppolo@polito.it

Model description

The aim is the simulation of evolution of dispersed magnetic nanoparticles Fe_3O_4 NPs upon the application of a magnetic field. In particular, their self-assembly into chains and their spatial rotation. Hence, the modeling of the Fe_3O_4 NPs by superparamagnetic NPs and the absence of the fluid. The model of interaction between NPs is described in the supplementary information of Ref. [1]. A system of 1,000 (thousand) NPs, with a diameter d, in a cube of side-length $L \times d$ was chosen to reproduce the experimental NPs weight fractions. L is equal to 50.53, 39.88, 34.65, and 31.3 for 2, 4, 6, and 8 wt.%, respectively. For a given external magnetic induction, the equilibrium self-assembly of NPs is obtained by minimizing the total energy of the system through the Evans and Beeler procedure [2,3]. In Figure S1, the simulated panels in d) and e) are the equilibrium configurations obtained, from randomly distributed NPs, when the magnetic field is applied horizontally and after the rotation of the magnetic direction by 30°, respectively.

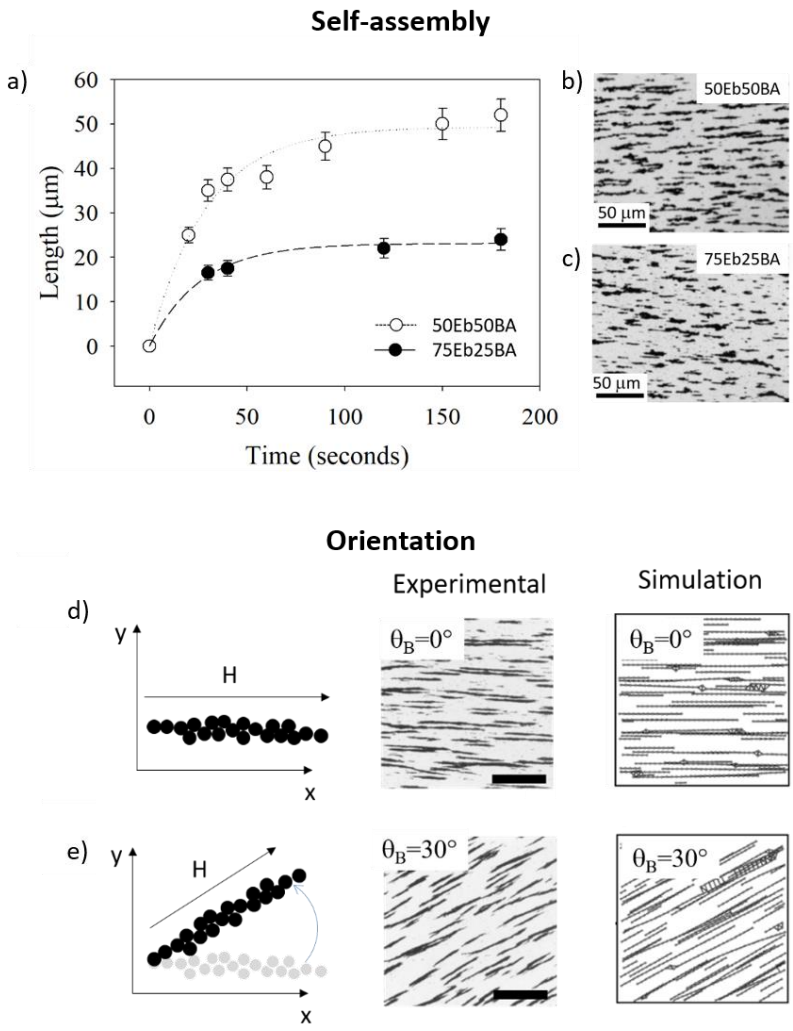

Figure S1: a) Experimental evolution of the length of the chains of Fe_3O_4 NPs for the two used formulations: 50Eb50BA (open circle) and the 75Eb25BA (full circle). Optical micrographs after 180 s for b) 50Eb50BA and c) 75Eb25BA formulations. Comparison between experimental observation and simulations for two different configurations of the microstructure. The latter is embedded in the 50Eb50BA formulation and triggered by applying a 10 mT magnetic field oriented d) at θ_B=0°, and e) at θ_B=30°, respectively. (Experimental scale bar is 50 μm and a 4.35×4.35×4.35 μm^3 cubic box is employed for the simulation.)

Magnetic properties

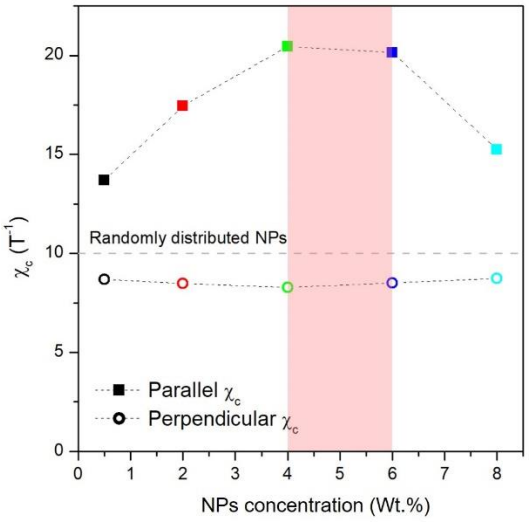

Figure S2. Parallel (square symbol) and perpendicular (circle symbol) magnetic susceptibility (χ_c) at the coercive field of the 75Eb25BA sample with self-assembled chains as a function of NPs concentrations. The value of χ_c corresponding to the randomly distributed NPs (gray dashed line) is used as reference.

The hysteresis loops reported in Fig. 4 b-e in the main text describe the magnetization process of the samples taking into account the effect of the demagnetizing field (H_d). Such an H_d field is proportional to the magnetization M by means of the demagnetizing factor (N_d) which is strongly correlated to the shape of the NPs microstructure. To infer the magnetic behavior independently from the H_d field contribution, the applied magnetic field (H) should be properly corrected: $H_{tr} = H - H_d = H - MN_d$.

Figure S3 shows the experimental hysteresis loop of the 75Eb25BA_6NPs sample containing a random dispersion of magnetic fillers (green solid curve) compared to the same hysteresis loop after the correction from the demagnetization field (blue dashed curve). The three components of the demagnetizing factors are taken equal ($N_{d\text{-}x} = N_{d\text{-}y} = N_{d\text{-}z} = 1/3$) due to the isotropic magnetic behavior of this sample (see Fig. 4 and relative discussion in the main text).

This corrected hysteresis loop is used as a reference curve in an *ad-hoc* iterative procedure to estimate the components of the N_d factors for the other samples containing a chain-like microstructure. In particular, the chains are modeled as prolate ellipsoids whose major axis is aligned along the x-direction ($N_{d\text{-}x} > N_{d\text{-}y} = N_{d\text{-}z}$). The estimation is considered satisfactory when

the corrected hysteresis loops (measured along the three axes of symmetry) of the samples containing a chain-like microstructure are well superimposed on the reference curve. Figure S3b is representative of all the studied samples. The estimated demagnetizing factor is related to the average aspect ratio of the chains (α) and to the anisotropy constant (K_s) by means of well-known equations [4]. Figure S3c summarizes the α and K_s values for all studied samples as a function of the NPs concentration. More exhaustive details and explanations about the demagnetizing field and the shape anisotropy can be found in the literature [4, 5].

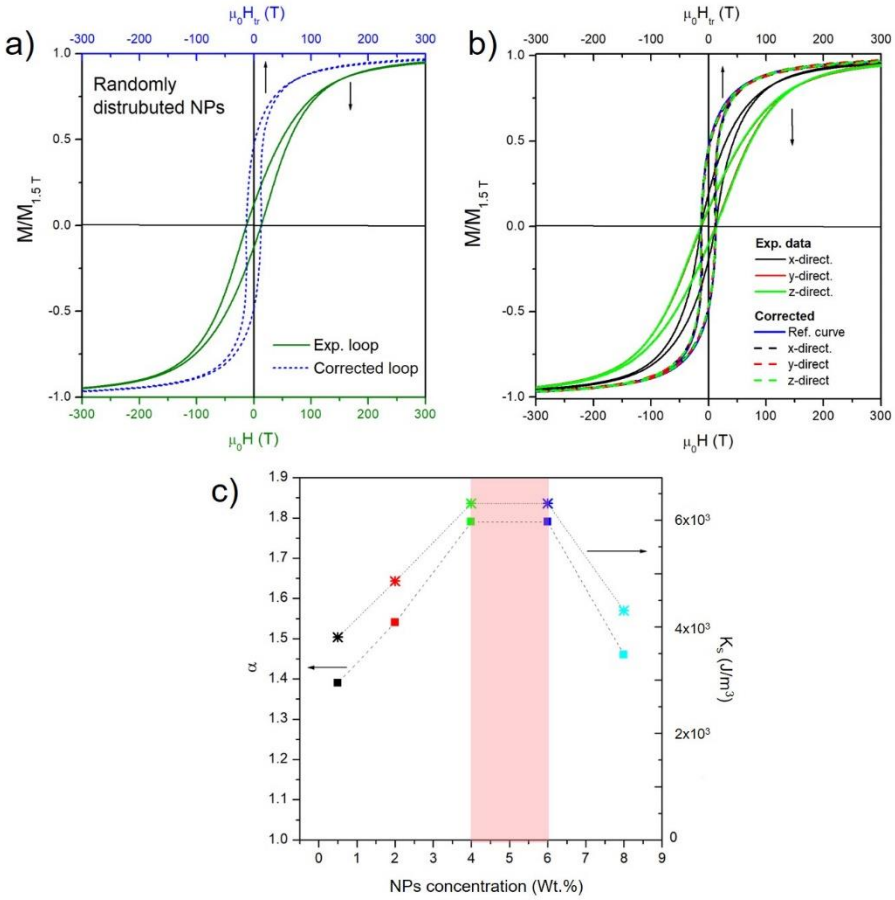

Figure S3:a) Hysteresis loops for a sample with a random dispersion of Fe_3O_4 nanoparticles (75Eb25BA_6wt%NPs): experimental curve (green solid line); the same curve after the correction from the H_d (blue dashed line); b) hysteresis loops of a sample containing a chain-like microstructure (75Eb25BA_6wt%NPs): experimental curves along the three symmetry directions (solid lines); the same curves after the correction from the H_d (dashed lines) superimposed to the reference curve (solid blue line); c) average aspect ratio (α, square symbol) and shape anisotropy constant (K_s, asterisk symbol) of the chains embedded in the polymer composite as a function of NPs concentration.

Mechanical properties

For each experimental configuration, four measurements have been performed and the elastic modulus has been obtained considering the slope of the curves in the elastic deformation region, i.e., $E = (Stress/Strain)_{Elastic\ region}$.

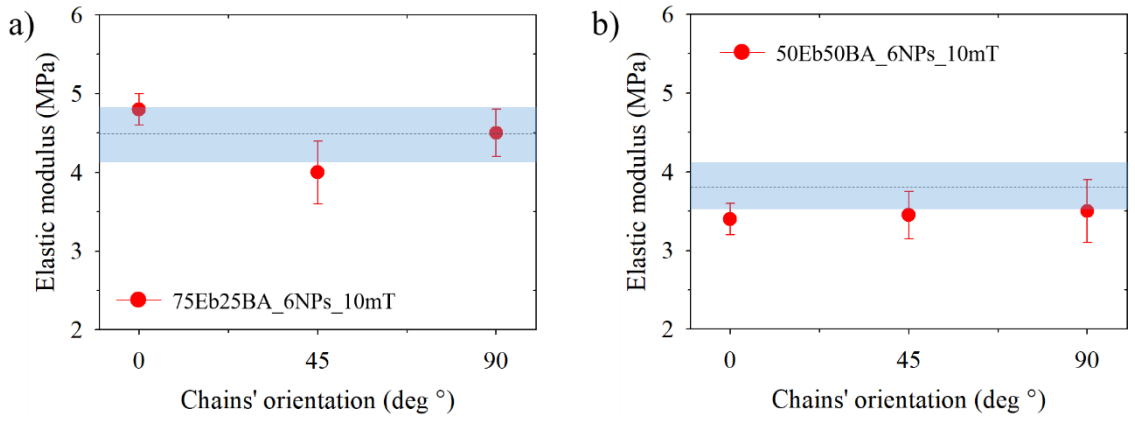

Figure S4. Evolution of the elastic modulus (E) as a function of the orientation of the chains for a) 75Eb25BA_6NPs_10mT and b) 50Eb50BA_6NPs_10mT samples. In each graph, the dotted line represents the elastic modulus measured for homogeneously dispersed specimens and the blue band the dispersion error range for that value.

The Helmholtz Coils setup

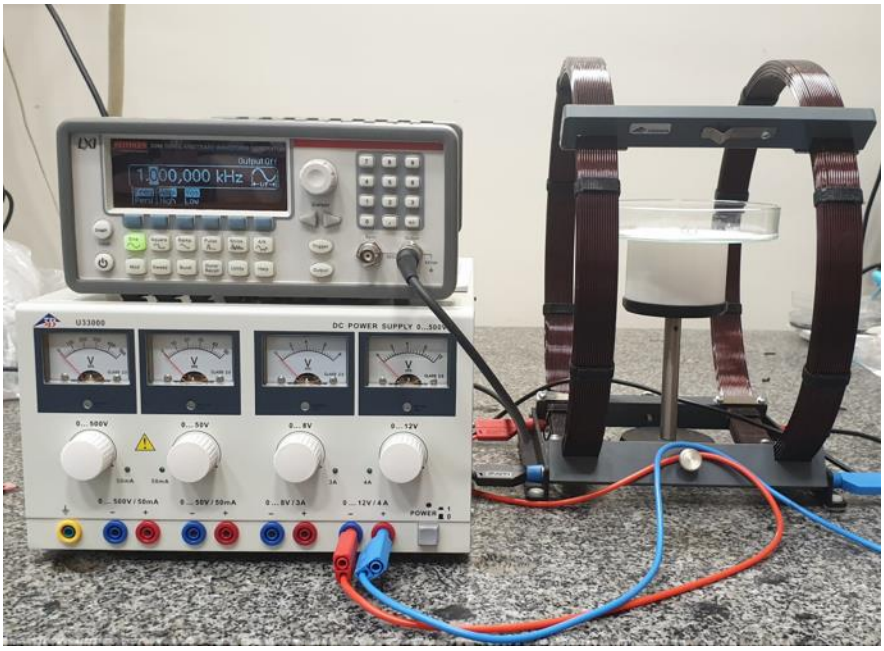

Figure S5: Experimental setup composed by Helmholtz coils used to test the magnetic devices.

Magneto-responsive gears

One gear (see geometry in Fig. S6a,b) contains randomly dispersed NPs and is used as a reference (Fig. S6c), while the second gear contains an oriented magnetic microstructure (Fig. S6d). At the beginning of the experiment, the magnetic field is switched off (H=0) and the initial orientation of the two gears is defined by the white spots and the blue arrows as shown in Fig. S6e. As the magnetic field (H=+4 mT) is applied in the direction indicated by the arrow in Fig. S6f, the spur gear containing the oriented chains undergoes a rotation to align the microstructure along the direction of H. Conversely, the spur gear containing only dispersed NPs remains approximately at the initial position. Once the equilibrium is reached, the direction of the magnetic field is reversed, i.e., H=-4 mT (Fig. S6g). Again, the spur gear containing the oriented chains flips about 180° to align itself along the new direction of H, whereas the one with dispersed NPs is not affected.

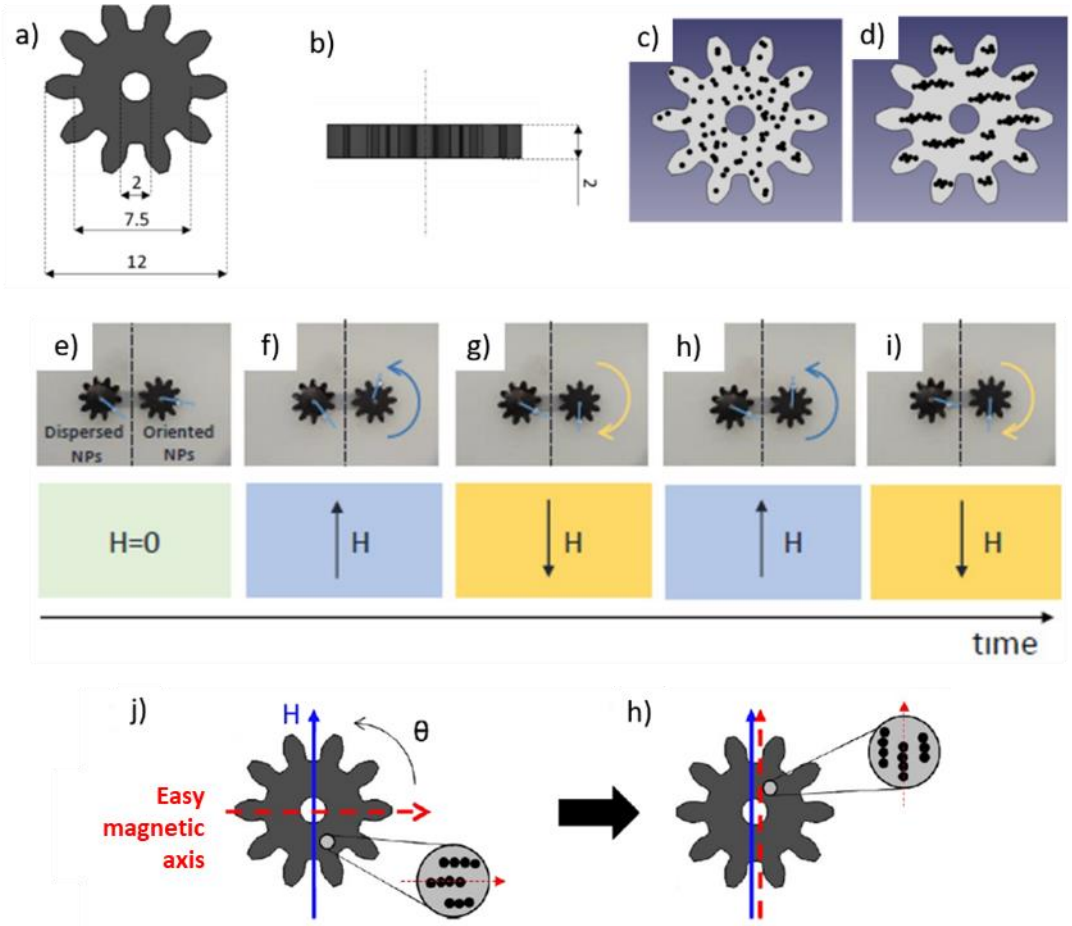

Figure S6: a-b) CAD file of the gear. Dimensions are in mm. Sketch of gear containing c) randomly dispersed NPs and d) an oriented magnetic microstructure. e) Initial configuration (H=0) for the two systems. Gear containing dispersed NPs is on the left, whereas gear containing the microstructure is on the right. f-g) Timeframe evolution of the two gears for different orientations of the applied magnetic field (H=±4 mT). j-h) Graphical representation of the rotation of the gear as it orients its microstructure along the direction of the applied field.

In a gear train, the rotational speed of the output (driven) gear depends on the driven-to-drive ratio, and it is expressed as a gear ratio [6]:

$$Gear\ ratio = \frac{Teeth\ number\ (driven)}{Teeth\ number\ (drive)} = \frac{Angular\ velocity\ (drive)}{Angular\ velocity\ (driven)}$$

For gear ratio >1, the driver gear is smaller than the driven gear and the latter rotates slower, but it also generates a higher torque. On the contrary, if the driver gear is larger than the driven one, the gear ratio is <1, and the driven gear rotates faster but with a lower torque. In our experiment, the gear ratio has been set to 2, such that the angular velocity of the driven gear is two times smaller

than that of the magneto-responsive drive gear, i.e., the drive gear is composed of 10 teeth, while the driven gear has 20 teeth. The gear train system was placed in a petri dish filled with water and anchored to a printed system composed of two plastic pinions and exposed to a rotating magnetic field (0-1 Hz). The timeframe evolution of the magneto-responsive gear train shown in Figs. S7b-f indicates that the drive wheel successfully transfers the momentum to the driven wheel demonstrating, in turn, the possibility to develop more complex magnetic driven-devices.

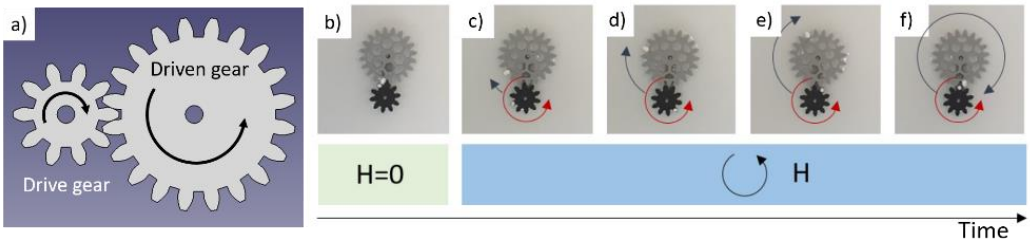

Figure S7: a) CAD file of a conventional gear train. b-f) Timeframe evolution of the magnetically-driven train-gear mechanism. White spots indicate the relative angular position of the two gears.

Magneto-responsive linear actuator

The proposed actuator is designed to transform a rotational motion into a linear one. Thus the spur gear rotates on a fixed axis, while the rack can move in the plane as shown in Fig. S8a. Our linear actuator is composed of a non-magnetic double-side rack (15 teeth, 1 mm module, 1 mm thick, and 47 mm long) and two spur gears (15 teeth, 1 mm module, and 2 mm thick), one of which is magneto-responsive and used as a drive gear, and the other one non-magnetic and used to stabilize the rack in its linear movement, Fig. S8b. The linear actuator is placed in a petri dish filled with water and anchored to a printed system composed of four pinions allowing the spur gears to rotate and the rack to move in the plane.

Once the field is applied, the anti-clockwise rotation of the magneto-responsive spur gear (indicated by the white spot) induces the displacement of the rack downwards (indicated by the arrow), Figs. S8c-d. The inversion of the field reverses the direction of rotation of the drive gear, which becomes clockwise. In this case, the rack moves upwards, Fig. S8e.

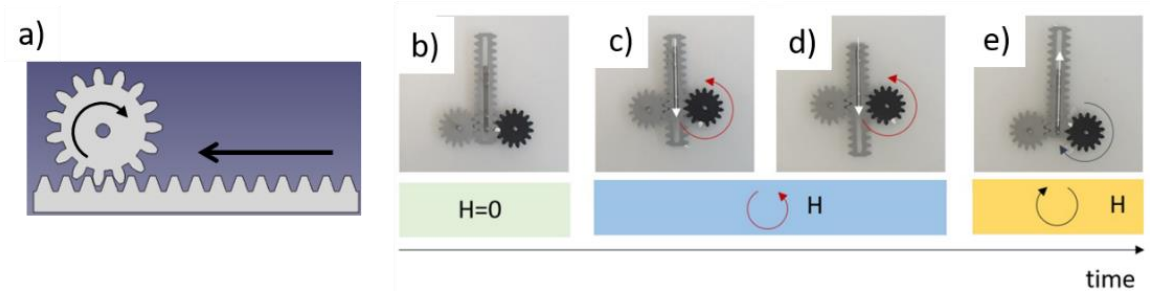

Figure S8. a) CAD file for a linear actuator composed of a gear and a rack. b-d) Timeframe evolution of the magnetically-driven linear actuator. White spot indicates the relative angular position of the magneto-responsive drive gear, whereas the white arrow indicates the direction of movement of the rack for the two directions of the applied field, c-d) anti-clockwise and e) clockwise.

References

1. S. Lantean, I. Roppolo, M. Sangermano, M. Hayoun, H. Dammak, G. Rizza, *Addit. Manuf.* **2021**, *47*, 102343, DOI 10.1016/J.ADDMA.2021.102343.
2. C.H. Bennett, Exact Defect Calculations in Model Substances, in: Diffusion in Solids, Ed. A.S. Nowick, J.J. Burton, Elsevier, 1975, 73-113. DOI 10.1016/b978-0-12-522660-8.50007-6.
3. J.R. Beeler, Jr, R.E. Dahl, Jr, R.D. Bourquin, *J. Phys. Colloq.* **1975**., 36, C4-97-C4-109, DOI 10.1051/jphyscol:1975411.
4. B. D. Cullity, C. D. Graham, *Introduction to Magnetic Materials*, **2008**. Copyright Institute of Electrical and Electronics Engineers DOI 10.1002/9780470386323.
5. J. M. D. Coey, *Magnetism and Magnetic Materials*, Cambridge University Press **2009**. DOI 10.1017/CBO9780511845000
6. R. K. Mobley, "Vibration Fundamentals," in Plant Engineer's Handbook, **2001**, Copyright Elsevier, DOI 10.1016/b978-075067328-0/50045-8.